Available online at www.sciencedirect.com
ScienceDirect
Ceramics International 37 (2011) 1525–1531
CERAMICS INTERNATIONAL
www.elsevier.com/locate/ceramint

Synthesis and electrical conductivity of La–Sr–X–Mg–O (X = Ti, Zr, Al) perovskite solid solution

Kentaro Shiratani, Yoshihiro Hirata *, Soichiro Sameshima, Naoki Matsunaga, Satoko Nakahara

Department of Chemistry, Biotechnology, and Chemical Engineering, Kagoshima University, 1-21-40 Korimoto, Kagoshima 890-0065, Japan

Received 25 October 2010; received in revised form 16 December 2010; accepted 9 January 2011
Available online 23 February 2011

Abstract

Perovskite solid solutions of $(La_{0.6}Sr_{0.4})(X_{1-y}Mg_y)O_{3-\delta}$ (X = Ti, Zr, Al) were prepared by a coprecipitation method using corresponding aqueous solutions and ammonium carbonate solution. The freeze-dried powders were sintered in air at 1000–1500 °C for 1–36 h. Single phase solid solutions were produced in the compositions of $(La_{0.6}Sr_{0.4})(Zr_{0.6}Mg_{0.4})O_{3-\delta}$ and $(La_{0.6}Sr_{0.4})(Al_{0.9}Mg_{0.1})O_{3-\delta}$ where $(3-\delta)<3$. For the compositions of X = Ti and Zr for $y = 0.1$ where $(3-\delta)>3$, two phases including perovskite solid solution were produced at 1400–1500 °C. The stability of perovskite solid solution was closely related to the fraction of lattice oxygen atom $(3-\delta)$. A relatively high conductivity was measured for $(La_{0.6}Sr_{0.4})(Al_{0.9}Mg_{0.1})O_{3-\delta}$ ($\sigma = 4.15\times10^{-4}$ S/cm at 600 °C, activation energy 113.4 kJ/mol). The influence of fraction of oxide ion vacancy on the activation energy was small for $\delta = 0.1$–0.3 of perovskite solid solution.

Keywords: A. Sintering; C. Electrical conductivity; D. Perovskites

1. Introduction

Solid electrolytes with high oxide ion conductivities are needed to operate an intermediate temperature solid oxide fuel cell (SOFC). The possible candidate electrolytes are doped-$LaGaO_3$ [1], $Zr_{1-x}Sc_xO_{2-(x/2)}$ (scandium-stabilized zirconia, ScSZ) and $Ce_{1-x}RE_xO_{2-(x/2)}$ (rare earth-doped ceria, RDC) [2–6]. Perovskite structure solid solutions with compositions of $(A_{1-x}A'_x)(B_{1-y}B'_y)O_{3-\delta}$ like doped-$LaGaO_3$ (A, A′: A-site cations coordinated by twelve oxide ions, B, B′: B-site cations coordinated by six oxide ions) are attractive oxide ion conductor. Doping of Sr^{2+} and Mg^{2+} ions to A-site and B-site of $LaGaO_3$, respectively, creates oxide ion vacancy and the oxide ion conductivity increases because the flux of oxide ions diffusing through oxide ion vacancies increases [1]. When a transition metal (for sample, Mn, Fe, Co) is doped at B-site, charge neutrality is maintained by change of the valence of B site cation. This phenomenon is not adequate to increase the oxide ion transference number. In our recent article [7], the electrical conductivity of $(La_{0.6}Sr_{0.4})(Ru_{1-y}Mg_y)O_{3-\delta}$ ($y = 0$–0.6) perovskite solid solution was measured at 400–800 °C in an oxygen pressure range from 10 to 10^{-14} Pa. The compositions of $y = 0$–0.3 provided the high conductivities of 19–360 S/cm in air at 800 °C due to hole conduction mechanism of B site cation ($Ru_2O_3 + Vo^{\bullet\bullet} + 1/2O_2 \rightarrow 2Ru_{Ru}{}^{\times} + 2h^{\bullet} + 4O_o{}^{\times} \rightarrow 2Ru_{Ru}{}^{\bullet} + 4O_o{}^{\times}$). The rigid valence of A and B cations is expected to achieve a high oxide ion conductivity. In this article, new perovskite solid solutions of $(La_{0.6}Sr_{0.4})(X_{1-y}Mg_y)O_{3-\delta}$ with stable valence of A and B site cations were synthesized for X = Al, Ti and Zr. Large cations of La (0.136 nm radius) and Sr (0.144 nm radius) [8] were placed on A site position to increase the volume of unit cell, which allows the easy migration of oxide ions. In this paper, following notation is used to express the metal and composition: LSTM6491 = $(La_{0.6}Sr_{0.4})(Ti_{0.9}Mg_{0.1})O_{3-\delta}$, LSZM6491 = $(La_{0.6}Sr_{0.4})(Zr_{0.9}Mg_{0.1})O_{3-\delta}$, LSZM6464 = $(La_{0.6}Sr_{0.4})(Zr_{0.6}Mg_{0.4})O_{3-\delta}$, and LSAM6491 = $(La_{0.6}Sr_{0.4})(Al_{0.9}Mg_{0.1})O_{3-\delta}$.

2. Experimental procedure

Aqueous solutions (0.2 M) of $La(NO_3)_3{\cdot}6H_2O$ (purity > 99.9 mass%), $Sr(NO_3)_2$ (purity > 98 mass%), $TiCl_4$ solution (purity, 16.0–17.0 mass%), $ZrOCl_2{\cdot}8H_2O$ (purity > 99.0 mass%), $Al(NO_3)_3{\cdot}9H_2O$ (purity > 99.9 mass%) and

* Corresponding author. Tel.: +81 99 285 8325; fax: +81 99 257 4742.
E-mail address: hirata@apc.kagoshima-u.ac.jp (Y. Hirata).

0272-8842/$36.00
doi:10.1016/j.ceramint.2011.01.027

$Mg(NO_3)_2{\cdot}6H_2O$ (purity > 99 mass%) were mixed with ammonium carbonate solution (0.2 M) to make coprecipitate of given compositions. The freeze-dried powders were heated at 1000–1500 °C for 1–48 h in air (SPM 6512 electric furnace, Marusho Electro-Heat Co. Ltd., Japan). The phases produced in heated samples were identified by X-ray diffraction (RINT2200, Rigaku Denki Co. Ltd., Japan). The lattice parameters of phases produced were calibrated with the diffraction angles of Si (purity > 99.99 mass%, Mitsuwa Chemical Industries Ltd, Japan) as an internal standard. LSTM6491, LSZM6491, LSZM6464 and LSAM6491 powders were compacted by uniaxial pressing at 49 MPa, followed by cold isostatic pressing (CIP) at 294 MPa to a disk with sizes of 10 mm diameter and 2 mm thickness, respectively. The compacts were sintered at 1000–1500 °C for 1–36 h in air and the sintered density was measured by the Archimedes method using double distilled water. The complex impedance of sintered compact was measured in a temperature range from 300 to 800 °C by a two-terminal AC bridge with LCR meter (E4980A, Agilent Technologies) at 100 Hz–2 MHz. Surfaces of a disk sample were polished with diamond paste of 1 μm. Au paste (TR-1301, Tanaka Kikinzoku Kogyo Co., Japan) was spread homogeneously on the polished disk sample and heated to 850 °C for 2 h to contact Pt electrodes.

3. Results and discussion

3.1. Preparation and crystal structure of La–Sr–X–Mg–O system

Fig. 1 shows typical X-ray diffraction patterns of La–Sr–X–Mg–O heated at 1000–1500 °C. In LSZM6464 composition, a nearly single phase solid solution (Fig. 1c) identified as orthorhombic $SrZrO_3$ perovskite (ICDD card 40-0161) was produced by heating at 1400–1500 °C for 10–24 h. At 1200–1300 °C, unknown phase coexisted with $SrZrO_3$ phase. Similarly, LSAM6491 composition heated at 1500 °C for 10–36 h (Fig. 1d) provided a nearly single phase of hexagonal $LaAlO_3$ (ICDD card 09-0072). On heating for 1 h at 1300–1500 °C, multi phases such as tetragonal $LaSrAl_3O_7$ (ICDD card 50-1815), tetragonal $SrLaAlO_4$ (ICDD card 24-1125) and monoclinic $SrAl_2O_4$ (ICDD card 34-0379) were produced together with $LaAlO_3$. However, no single phase of perovskite structure was produced in the compositions of LSTM6491 and LSZM6491 under the present heating conditions at 1000–1500 °C for 1–48 h. As seen in Fig. 1a, heating of LSTM6491 at 1000–1100 °C resulted in two phases of cubic $SrTiO_3$ (ICDD card 35-0734) and hexagonal La_2O_3 (ICDD card 05-0602). Further heating at 1200–1400 °C for 1–4 h produced $La_2Ti_2O_7$ or $La_{0.5}Mg_{0.5}Ti_{3.5}O_{15}$, together with $SrTiO_3$ and La_2O_3. In LSZM6491 composition (Fig. 1b), two phases of orthorhombic $SrZrO_3$ and cubic $La_2Zr_2O_7$ were identified under the wide heating conditions at 1000–1500 °C for 1–48 h. The above phase relations are discussed in a latter part (Table 1, Fig. 2) and related to the composition of lattice oxygen. The lattice oxygen compositions, $3-\delta$, are calculated to be 3.2, 3.2, 2.7 and 2.75 for LSTM6491, LSZM6491, LSZM6464 and LSAM6491, respectively. The compositions of $(3-\delta) < 3$ (LSZM6464 and LSAM6491) of oxide ion vacancy provided a single phase perovskite. However, the systems with $(3-\delta) > 3$ lead to the formation of interstitial oxygen atom. This type of perovskite structure with excess oxygen atom is unstable and decomposes into stable two phases.

The stability of perovskite solid solution is discussed according to a virtual quaternary phase system of $SrMgO_2$–$SrXO_3$–$LaXO_{3.5}$–$LaMgO_{2.5}$. The *y*-axis and *x*-axis in Fig. 2 indicates the fractions of La at A-site and X at B-site of perovskite structure, respectively. As seen in Fig. 2, LSXM 6491 composition may be formed from three end compositions of $LaMgO_{2.5}$–$SrXO_3$–$LaXO_{3.5}$ (region I) or $SrMgO_2$–$SrXO_3$–$LaXO_{3.5}$ (region II). Similarly, LSXM6464 composition can be divided into two end compositions of $SrMgO_2$–$LaXO_{3.5}$ or

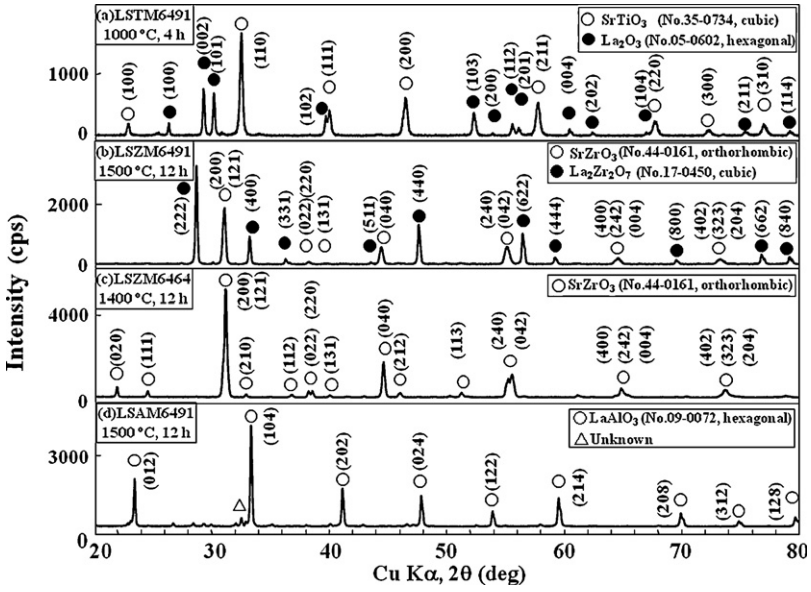

Fig. 1. Typical X-ray diffraction patterns of La–Sr–X–Mg–O system heated at 1000–1500 °C in air.

Table 1
Phases and fractions in quaternary phase system for $(La_{0.6}Sr_{0.4})(X_{1-y}Mg_y)O_{3-\delta}$.

Sample	X	y	Regions in Fig. 2		mol% of phases		Phases by XRD
LSTM6491-1400	Ti (1400 °C, 4 h)	0.1	I	$SrTiO_3$	62.50		$SrTiO_3 + La_5Mg_{0.5}Ti_{3.5}O_{15}$
				MgO	6.25	$Sr_{0.77}(Ti_{0.92}Mg_{0.077})O_{2.69}$ 81.25	
				TiO_2	12.5		
				$La_5Mg_{0.5}Ti_{3.5}O_{15}$	18.75		
	Ti (1400 °C, 4 h)	0.1	II	$SrTiO_3$	51.72		$SrTiO_3 + La_5Mg_{0.5}Ti_{3.5}O_{15}$
				MgO	5.17	$Sr_{0.68}(Ti_{0.93}Mg_{0.068})O_{2.61}$ 75.86	
				TiO_2	18.97		
				$(La_{4.29}Sr_{0.71})(Ti_{3.5}Mg_{0.5})O_{13.93}$	24.14		
LSTM6491-1000	Ti (1000 °C, 4 h)	0.1	I, II	$SrTiO_3$	30.77		$SrTiO_3 + La_2O_3$
				MgO	7.69	$Sr_{0.4}(Ti_{0.9}Mg_{0.1})O_{2.3}$ 76.92	
				TiO_2	38.46		
				La_2O_3	23.08		
LSZM6491-1500	Zr (1500 °C, 12 h)	0.1	I	$(La_{0.2}Sr_{0.8})(Zr_{0.8}Mg_{0.2})O_{2.9}$	66.67		$SrZrO_3 + La_2Zr_2O_7$
				$La_2Zr_2O_7$	33.33		
	Zr (1500 °C, 12 h)	0.1	II	$Sr(Zr_{0.75}Mg_{0.25})O_{2.75}$	57.14		$SrZrO_3 + La_2Zr_2O_7$
				$La_2Zr_2O_7$	42.86		
LSZM6464-1400	Zr (1400 °C, 12 h)	0.4	I	$(La_{0.6}Sr_{0.4})(Zr_{0.6}Mg_{0.4})O_{2.7}$ ($La_2Zr_2O_7$–$SrMgO_2$ system)	100		$SrZrO_3$
LSAM6491-1500	Al (1500 °C, 12 h)	0.1	I, II	$(La_{0.6}Sr_{0.4})(Al_{0.9}Mg_{0.1})O_{2.75}$	100		$LaAlO_3$

three end compositions of region I. Table 1 summarizes the calculated fractions and compositions of phase of La–Sr–X–Mg–O system. For example, $SrTiO_3$ and La_2O_3 were identified in LSTM6491 composition (Fig. 1a) by heating at 1000 °C for 4 h in air. The analysis of LSTM6491 in region I provided the composition of 0.4 mol $SrTiO_3$–0.25 mol $La_2Ti_2O_7$–0.1 mol $LaMgO_{2.5}$ = 30.77 mol% $SrTiO_3$–7.69 mol% MgO–38.46 mol% TiO_2–23.08 mol% La_2O_3. Since the produced phases provided X-ray diffraction patterns of $SrTiO_3$ and La_2O_3, the above calculated fractions of oxide components were assigned to form $Sr_{0.4}(Ti_{0.9}Mg_{0.1})O_{2.3}$ solid solution plus La_2O_3. That is, the analysis of LSTM6491 in both region I and II provides the two phases of 76.92 mol% $Sr_{0.4}(Ti_{0.9}Mg_{0.1})O_{2.3}$–23.08 mol% La_2O_3 and agreed with qualitatively the measured phases. A similar analysis in Table 1 explains well the identified phases. The interesting result in Table 1 is that the lattice oxygen composition $(3-\delta)$ of perovskite solid solution is smaller than 3 and suggests that no interstitial oxygen atom is included in the perovskite formed.

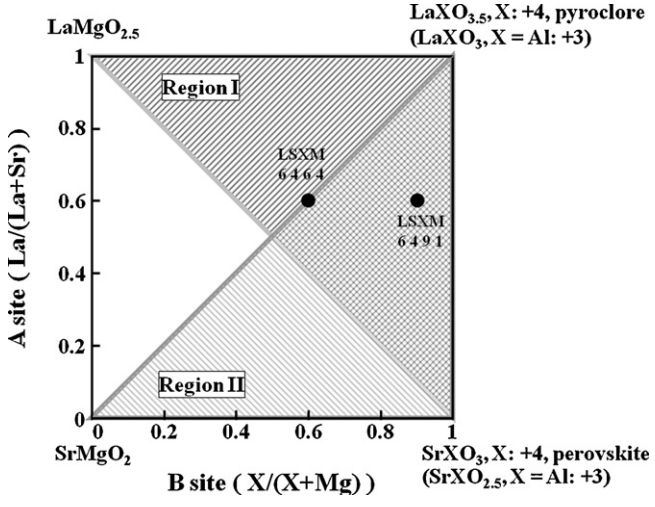

Fig. 2. Quaternary phase relation for $(La_{1-x}Sr_x)(X_{1-y}Mg_y)O_{3-\delta}$.

Table 2 shows the density calculated from the measured lattice parameters, fractions and compositions of phases analyzed in Table 1. For example, 5.596 and 5.523 g/cm^3 were calculated for the analysis of phases in region I and II of LSZM6491-1500 sample, respectively. The bulk and apparent densities of sintered disk were measured to be 3.507 and 5.795 g/cm^3, respectively. The comparison of measured and calculated densities indicates that (1) the calculated density in region I is closer to apparent density and (2) apparent density (containing closed pores) is higher than bulk density (containing both open and closed pores). That is, most of pores in the sintered disk were open pores and as a result the calculated density was close to apparent density (≈true density, containing no pores). The ratio of bulk density to apparent density was 60.5% and low sinterability was measured. A similar tendency was also seen for LSTM6491 and LSZM6464 in Table 2. On the other hand, the measured densities of LSAM6491 indicate the formation of dense structure because of the similar values of bulk density ≈ apparent density ≈ calculated density. The above results were compared

Table 2
Crystal structure, lattice parameters and density of phases produced.

Sample	Phase	Crystal structure	Lattice parameter/nm (unit cell volume/nm^3)	Density (g/cm^3)		
				Calculated	Measured	
LSTM6491 -1000	$Sr_{0.4}(Ti_{0.9}Mg_{0.1})O_{2.3}$ (76.92 mol%)	Cubic	$a = b = c = 0.3895$ ($V = 0.0591$)	3.297 } 4.262 (mixed) 6.573 }	3.339 (Bulk)	3.957 (apparent)
	La_2O_3 (23.08 mol%)	Hexagonal	$a = b = 0.3936$ $c = 0.6136$ ($V = 0.2767$)		(84.4% relative density)	
LSZM6491 -1500	$(La_{0.2}Sr_{0.8})(Zr_{0.8}Mg_{0.2})O_{2.9}$ (I: 66.67 mol%) $Sr(Zr_{0.75}Mg_{0.25})O_{2.75}$ (II: 57.14 mol%)	Orthorhombic	$a = 0.5810$ $b = 0.8205$ $c = 0.5785$ ($V = 0.2758$)	I : 5.349 } I : 5.596 II : 5.021 } II : 5.523 5.803 } (mixed)	3.507 (Bulk)	5.795 (apparent)
	$La_2Zr_2O_7$ (I: 33.33, II: 42.86 mol%)	Cubic	$a = b = c = 1.0954$ ($V = 1.3145$)		(60.5% relative density)	
LSZM6464 -1400	$(La_{0.6}Sr_{0.4})(Zr_{0.6}Mg_{0.4})O_{2.9}$	Orthorhombic	$a = 0.5855$ $b = 0.8068$ $c = 0.5840$ ($V = 0.2759$)	5.520	3.676 (Bulk)	5.603 (apparent)
					(65.6% relative density)	
LSAM6491 -1500	$(La_{0.6}Sr_{0.4})(Al_{0.9}Mg_{0.1})O_{2.75}$	Hexagonal	$a = b = 0.5383$ $c = 1.259$ ($V = 0.3160$)	4.969	4.924 (Bulk)	5.030 (apparent)
					(97.9% relative density)	

with direct observation of sintered microstructures in Section 3.2.

3.2. Microstructures of La–Sr–X–Mg–O systems

Fig. 3 shows the microstructures of (a) LSTM6491 sintered at 1000 °C, (b) LSZM6491 sintered at 1500 °C, (c) LSZM6464 sintered at 1400 °C and (d) LSAM6491 sintered at 1500 °C, respectively. The microstructure of LSTM6491 consisted of bimodal grain sizes of about 2 μm and 0.1 μm. As shown in Table 2, LSTM6491 contained two phases of 76.92 mol% $Sr_{0.4}(Ti_{0.9}Mg_{0.1})O_{2.3}$ and 23.08 mol% La_2O_3. These phase fractions lead to the interpretation that fine grains are to be La_2O_3 and large grains are to be $SrTiO_3$ solid solution. Although LSZM6491-1500 (Fig. 3b) contained two phases of $SrZrO_3$ solid solution and $La_2Zr_2O_7$, it was difficult to distinguish one phase from another phase in the microstructure. The average grain size was 1.86 μm for the microstructure of Fig. 3b. The microstructures of Fig. 3c and d correspond to single phase $SrZrO_3$ solid solution of 1.42 μm average grain size and $LaAlO_3$ solid solutions of 0.65 μm average grain size, respectively. When the microstructures in Fig. 3 is compared with the corresponding relative density in Table 2, it is found that (1) sinterability increases in the following order of B site cation at a similar composition LSXM6491: Zr < Ti < Al, (2) the tendency between densification and grain growth is opposite and average grain size became larger in the following order of B site cation: Al < Ti < Zr, and (3) the sinterability of LSZM is almost independent of the composition.

3.3. Electrical properties of La–Sr–X–Mg–O solid solutions

Before the analysis of detailed mechanisms of electrical conduction, the conductivity of single phase or two phases La–Sr–X–Mg–O systems was measured by alternating current method in air as a first step. Figs. 4 and 5 show the typical complex impedance plots at 500 and 700 °C for LSTM6491-1000, LSZM6491-1500, LSZM6464-1400 and LSAM6491-1500 samples, respectively. The last number in sample name expresses sintering temperature. The impedance plots were fitted with the equivalent electrical circuit models presented as solid lines in Figs. 4 and 5. The measured data were well simulated by the proposed circuit models. The physical meaning of two or three semi circles is under investigation. The total sample resistance was determined from the real resistance at imaginary resistance = 0 at low frequency.

Fig. 6 shows the Arrhenius plots of total electrical conductivity of (a) LSTM6491-1000, (b) LSZM6491-1500, (c) LSZM6464-1400 and (d) LSAM6491-1500. In Fig. 6, the conductivities of related oxide ion conductors are also plotted [1,9–11]. At first, it is easy to analyze the single phase perovskite solid solutions of LSZM6464 and LSAM6491. The conductivities at 600 °C were 5.14×10^{-6} and 4.15×10^{-4} S/cm for porous LSZM6464 and dense LSAM6491, respectively. This value of LSAM6491 was about 1/100 of the ionic conductivity of $(La_{0.9}Sr_{0.1})(Ga_{0.8}Mg_{0.2})O_{3-\delta}$ [1], but compar-

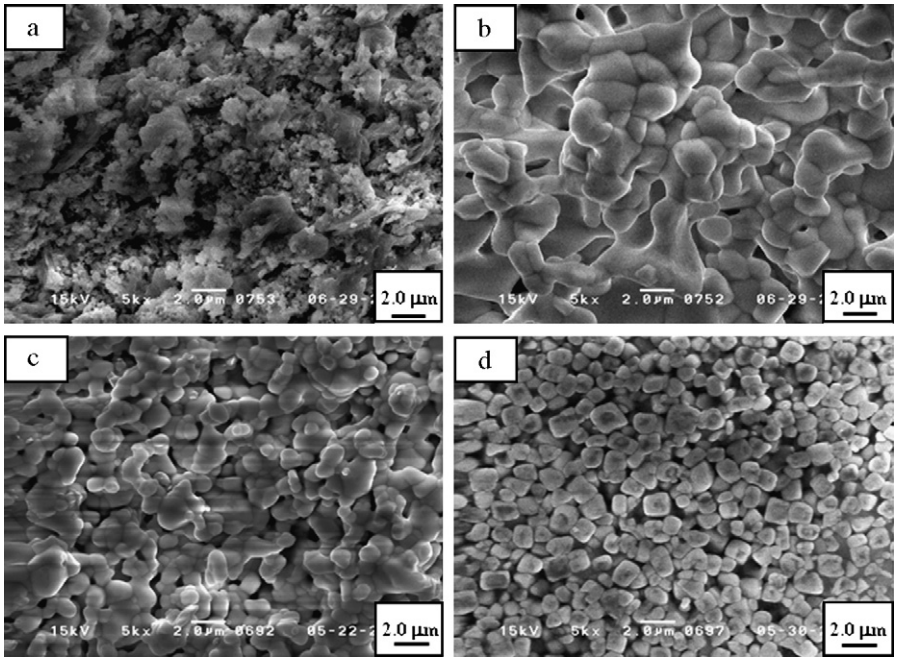

Fig. 3. Microstructures of (a) LSTM6491-1000, (b) LSZM6491-1500, (c) LSZM6464-1400 and (d) LSAM6491-1500. The last number of sample name indicates the sintering temperature.

able to the conductivity calcia-stabilized zirconia (CSZ) [9]. The activation energies of LSZM6464 (93.0 kJ/mol) and LSAM6491 (113.4 kJ/mol) were higher than that of $(La_{0.9}Sr_{0.1})(Ga_{0.8}Mg_{0.2})O_{3-\delta}$ (54 kJ/mol). LSZM6491 sintered at 1500 °C contained a perovskite solid solution and pyrochlore ($La_2Zr_2O_7$). Yamamura et al. [11,12] reported the hole conductivity and low activation energy (55 kJ/mol) for $La_2Zr_2O_7$. The conductivity of $La_2Zr_2O_7$ is also plotted in Fig. 6. The conductivity at 600 °C and activation energy of LSZM6491-1500 was 5.14×10^{-6} S/cm and 73.7 kJ/mol. The

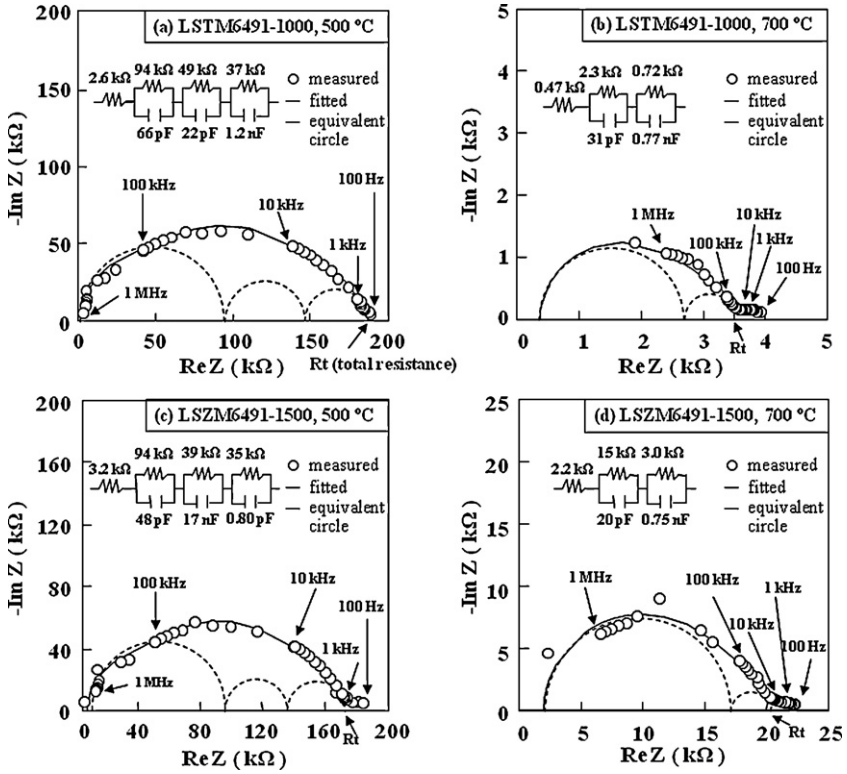

Fig. 4. Complex impedance plots of LSTM6491-1000 at (a) 500 °C and (b) 700 °C, and LSZM6491-1500 at (c) 500 °C and (d) 700 °C, respectively.

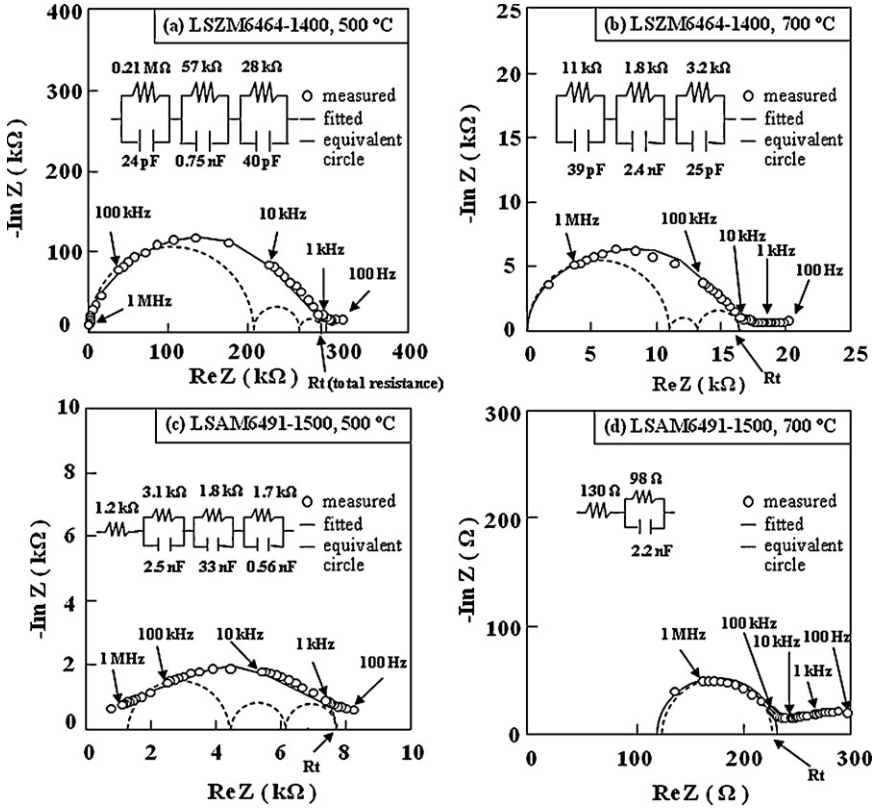

Fig. 5. Complex impedance plots of LSZM6464-1400 at (a) 500 °C and (b) 700 °C, and LSAM6491-1500 at (c) 500 °C and (d) 700 °C, respectively.

relatively high conductivity and low activation energy of porous LSZM6491-1500 may be due to the coexistence of $La_2Zr_2O_7$. LSTM6491 sintered at 1000 °C for 4 h contained La_2O_3 together with $SrTiO_3$ solid solution. Since La_2O_3 is an insulator, the conductivity of LSTM6491 depends on the fraction and relative density of $SrTiO_3$ perovskite solid solution. As seen in Fig. 6, the activation energy (128.8 kJ/mol) for $SrTiO_3$ solid solution was higher than that of LSAM6491.

Fig. 7 shows influence of average ionic radius of B-site cations on activation energy of perovskite solid solutions.

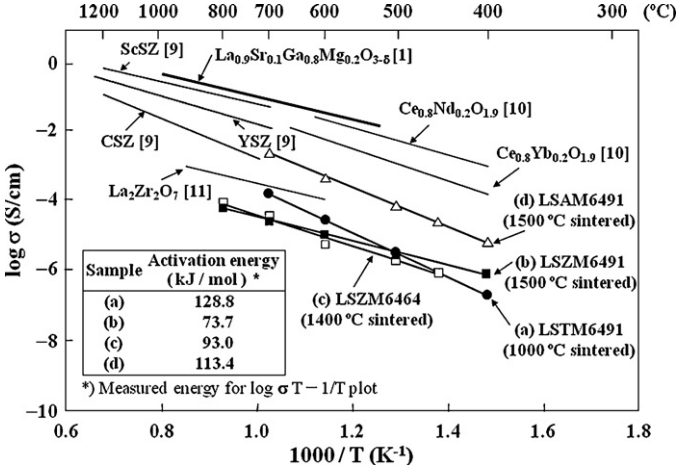

Fig. 6. Arrhenius plots of electrical conductivities of perovskite solid solutions and related oxide ion conductors.

The activation energies of LSZM6491-1500 ($(La_{0.2}Sr_{0.8})(Zr_{0.8}Mg_{0.2})O_{2.9}$–$La_2Zr_2O_7$), LSZM6464-1400 ($(La_{0.6}Sr_{0.4})(Zr_{0.6}Mg_{0.4})O_{2.75}$) and LSAM6491-1500 ($(La_{0.6}Sr_{0.4})(Al_{0.9}Mg_{0.1})O_{2.75}$) changed with the size of B-site cations. The activation energy for $LaAlO_3$ with no oxide ion vacancy is fairly high (181.4 kJ/mol) and the conductivity is low (4.17×10^{-5} S/cm at 600 °C) [13]. The activation energies of perovskite with $\delta = 0.1$–0.2 are also plotted as square marks in Fig. 7 [14]. These values were lower than 100 kJ/mol and showed a minimum at 0.062 nm of B site radius. The activation energies measured in this study ($\delta = 0.10$–0.30) showed a similar tendency except for $Sr_{0.4}(Ti_{0.9}Mg_{0.1})O_{2.3}$–$La_2O_3$ system ($\delta = 0.70$). The increase of activation energy with increasing fraction of oxide ion vacancy ($\delta = 0.70$ for $Sr_{0.4}(Ti_{0.9}Mg_{0.1})O_{2.3}$) is interpreted as follows. The measured activation energy consists of two kinds of energy: association of positively charged oxide ion vacancy ($V_O^{\bullet\bullet}$) and negatively charged dopant (for example, Sr_{La}', Mg_{Al}') and diffusion of oxide ion through oxide ion vacancy. The increased amount of dopant enhances the fraction of oxide ion vacancy and increases the coulombic attraction between these defects. The suppressed migration of oxide ion vacancy due to the increased coulombic attraction leads to the increased activation energy and decreases the conductivity. More measurement of the electrical conductivity in O_2-poor atmosphere will be continued to understand the conduction mechanisms of perovskite solid solutions.

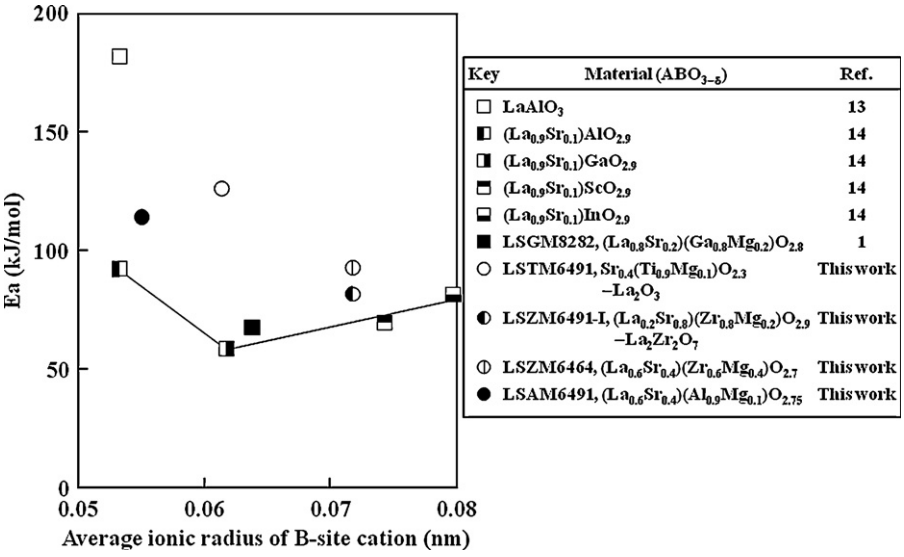

Fig. 7. Influence of average ionic radius of B-site cations of perovskite structure on activation energy of electrical conductivity.

4. Conclusions

(1) The oxide systems of $(La_{0.6}Sr_{0.4})(X_{1-y}Mg_y)O_{3-\delta}$ composition are stable for $(3-\delta) < 3$ upon heating at 1000–1500 °C in air. Single phase perovskite solid solutions were produced in the compositions of $(La_{0.6}Sr_{0.4})(Zr_{0.6}Mg_{0.4})O_{2.9}$ and $(La_{0.6}Sr_{0.4})(Al_{0.9}Mg_{0.1})\ O_{2.75}$.

(2) The oxide system of $(La_{0.6}Sr_{0.4})(X_{1-y}Mg_y)O_{3-\delta}$ composition is unstable for $(3-\delta) > 3$ upon heating at 1000–1500 °C in air. For the compositions of X = Ti and Zr for $y = 0.1$, two phases were produced at 1400–1500 °C: For example, $Sr_{0.77}(Ti_{0.92}Mg_{0.077})O_{2.69}$–$La_5Ti_{3.5}Mg_{0.5}O_{15}$, $Sr_{0.68}(Ti_{0.93}Mg_{0.068})O_{2.61}$–$(La_{4.29}Sr_{0.71})\ (Ti_{3.5}Mg_{0.5})O_{13.93}$ or $(La_{0.2}Sr_{0.8})(Zr_{0.8}Mg_{0.2})O_{2.9}$–$La_2Zr_2O_7$. These phases were analyzed in quaternary phase system for of $SrMgO_2$–$SrXO_3$–$LaXO_{3.5}$–$LaMgO_{2.5}$.

(3) A relatively high conductivity was measured for $(La_{0.6}Sr_{0.4})(Al_{0.9}Mg_{0.1})O_{2.75}$ composition ($\sigma = 4.15 \times 10^{-4}$ S/cm at 600 °C).

(4) The influence of fraction of oxide ion vacancy (δ in $O_{3-\delta}$) on the activation energy was small for $\delta = 0.1$–0.3.

Acknowledgements

This work was financially supported by Nippon Sheet Glass Foundation for Materials Science and Engineering (2010).

References

[1] T. Ishihara, H. Matsuda, Y. Takita, Doped $LaGaO_3$ perovskite type oxide as a new oxide ionic conductor, J. Am. Chem. Soc. 116 (9) (1994) 3801–3803.

[2] H. Inaba, H. Tagaka, Ceria-based solid electrolytes, Solid State Ionics 83 (1–2) (1996) 1–16.

[3] K. Eguchi, Ceramic materials containing rare earth oxides for solid oxide fuel cell, J. Alloys Compd. 250 (1–2) (1997) 486–491.

[4] Y. Hirata, S. Yokomine, S. Sameshima, T. Shimonosono, S. Kishi, H. Fukudome, Electrochemical properties of solid oxide fuel cell with Sm-doped ceria electrolyte and cermet electrodes, J. Ceram. Soc. Jpn. 113 (9) (2005) 597–604.

[5] M. Nagamori, T. Shimonosono, S. Sameshima, Y. Hirata, N. Matsunaga, Densification and cell performance of gadolinium-doped ceria (GDC) electrolyte/NiO–GDC anode laminates, J. Am. Ceram. Soc. 92 (S1) (2009) S117–S121.

[6] Y. Hirata, K. Matsumoto, S. Sameshima, N. Matsunaga, M. Nagamori, T. Shimonosono, Cell performance of strontium ruthenium oxide cathode/Gd-doped ceria (GDC) electrolyte/nickel-GDC anode system, J. Ceram. Soc. Jpn. 117 (11) (2009) 1141–1146.

[7] S. Sameshima, D. Moriyama, Y. Hirata. N. Matsunaga, Synthesis and electrical conductivity of $La_{0.6}Sr_{0.4}Ru_{1-x}Mg_xO_{3-\delta}$ ($x = 0$–0.6) perovskite solid solution, Mater. Chem. Phys., 125 2011 191-195.

[8] R.D. Shanon, Revised effective ionic radii and systematic studies of interatomic distances in halides and chalcogenides, Acta Crystallogr. A 32 (5) (1976) 751–767.

[9] C.B. Choundhary, H.S. Maiti, E.C. Subbarao, in: E.C. Subbarao (Ed.), Solid Electrolytes and Their Applications, Plenum Press, New York, 1980 p.40.

[10] N. Sakai, K. Yamaji, T. Horita, H. Yokokawa, Y. Hirata, S. Sameshima, Y. Nigara, J. Mizusaki, Determination of hydrogen solubility in oxide ceramics by using SIMS analyses, Solid State Ionics 125 (1–4) (1999) 325–331.

[11] H. Yamamura, H. Nishino, K. Kakinuma, K. Nomura, Electrical conductivity anomaly around fluorite–pyrochlore phase boundary, Solid State Ionics 158 (3–4) (2003) 359–365.

[12] H. Yamamura, H. Nishino, K. Kakinuma, K. Nomura, Crystal phase and electrical conductivity in the pyrochlore-type composition system, $Ln_2Ce_2O_7$ (Ln = La, Nd, Sm, Eu, Gd, Y and Yb), J. Ceram. Soc. Jpn. 111 (12) (2003) 902–906.

[13] T.L. Nguyen, M. Dokiya, S. Wang, H. Tagawa, T. Hashimoto, The effect of oxygen vacancy on the oxide ion mobility in $LaAlO_3$-based oxides, Solid State Ionics 130 (3–4) (2000) 229–241.

[14] K. Nomura, S. Tanase, Electrical conduction behavior in $(La_{0.9}Sr_{0.1})M^{III}O_{3-\delta}$ (M^{III} = Al, Ga, Sc, In, and Lu) perovskites, Solid State Ionics 98 (3–4) (1997) 229–236.